



Agricultural gas emissions during the spring thaw: Applying a new measurement technique

Thomas K. Flesch ^{a,*}, Vern S. Baron ^b, John D. Wilson ^a, David W.T. Griffith ^c,
John A. Basarab ^d, Peter J. Carlson ^a

^a Department of Earth and Atmospheric Sciences, University of Alberta, Edmonton, Canada

^b Agriculture and Agri-Food Canada, Lacombe, AB, Canada

^c Department of Chemistry, University of Wollongong, Wollongong, NSW, Australia

^d Alberta Agriculture and Forestry, Lacombe, AB, Canada



ARTICLE INFO

Article history:

Received 29 October 2015

Received in revised form 6 February 2016

Accepted 8 February 2016

Keywords:

Flux-gradient

Ground-air exchange

Inverse dispersion

FTIR

Open-path sensors

ABSTRACT

A new micrometeorological technique is applied to measure gas emissions from soils. The technique relies on a single open-path FTIR sensor (OP-FTIR) with motorized aiming to give gas concentrations along vertically separated paths (not necessarily parallel with each other). Emission rates are inferred from the vertical difference in concentration using two alternative methods: flux-gradient and inverse dispersion calculations. Our objective is to assess the capability of the technique in a field study measuring nitrous oxide (N_2O) and ammonia (NH_3) emitted from cattle overwintering areas during the spring thaw. Two field configurations were examined: a slant path configuration in which the OP-FTIR is aimed directly at high and low reflectors at the far end of the path (average vertical path separation ~ 1 m), and a periscope configuration where the lower FTIR path was directed closer to ground along the whole path (average path separation ~ 1.5 m). Measured emission rates were generally above the detectability threshold of the system and consistent with the scientific literature showing an emission rise during thawing. At one of our sites the pulse of N_2O emitted during thawing was among the largest reported ($9.9 \text{ kg N-N}_2\text{O ha}^{-1}$ during April). Of the two alternatives tested for calculating emissions, the inverse dispersion approach is more flexible, but with a computation time that can be prohibitive. With large measurement fetches the flux-gradient approach can be equally good and computationally faster. We conclude that the open-path gradient system provides a practical option for studying emissions in difficult environments.

© 2016 Elsevier B.V. All rights reserved.

1. Introduction

Long line-averaging open-path concentration sensors¹ measure gas concentration in the air between the sensor and a distant point. Here we consider so-called active systems, in which a beam of radiation (typically infrared) from an artificial source is sent to a reflector and the spectrum of the returning signal is analyzed for concentration information. These systems could be based on a tunable diode laser (TDL), Fourier transform infrared (FTIR), or differential optical absorption (DOAS) spectroscopy. With the potential for large measurement footprints, freedom from tubing

and pumping, and the ability for remote sampling, there is interest in how these sensors can be integrated into a micrometeorological methodology to provide new and more flexible ways to estimate gas emissions.

Open-path sensors paired with the mass balance principle (e.g., Desjardins et al., 2004) or with inverse dispersion techniques (e.g., Harper et al., 2010) have been widely used to make emission measurements. These are techniques naturally suited to line-average concentrations, and the pairing with open-path sensors works well for spatially discrete and small emission sources. Different micrometeorological techniques are typically used for spatially extensive sources such as agricultural fields or natural landscapes. These include eddy-covariance, flux-gradient, and relaxed eddy accumulation techniques. These techniques estimate the vertical flux of gas at a point above the emitting surface, which is typically equated to the underlying emission rate. The use of open-path sensors here is more problematic, e.g., eddy-covariance needs co-located concentration and turbulence information, information that is practically unattainable.

* Corresponding author at: Department of Earth and Atmospheric Sciences, University of Alberta, Edmonton, Canada T6E 2H4.

E-mail address: thomas.flesch@ualberta.ca (T.K. Flesch).

¹ We use “open-path” to designate long-pathlength measurements, where the extended 1-dimensional nature of the measurement is an explicit feature. This is in contrast to open-path sensors designed to approximate point measurements (e.g., folded path sensors).

A companion paper (Wilson and Flesch, 2016) investigated the use of open-path sensors in a flux-gradient (FG) type calculation, where emissions were deduced from a height difference in gas concentration. That paper considered horizontally overlapping but vertically separated measurement paths. This configuration is not a traditional FG application since the measurement paths are not necessarily parallel with the ground or with each other (which can be a useful configuration, e.g., a single sensor aimed to different reflectors). Wilson and Flesch showed that the procedure is moderately robust to non-parallel path alignments, uneven terrain, and a sensor located near (or even outside) the source area.

A concern with open-path concentration sensors in FG calculations is the sensitivity of the sensor. Unlike closed-path systems where the measurement environment can be manipulated to enhance sensitivity (e.g., reduced pressure, removal of competing constituents), open-path sensors have more severe sensitivity limitations. Consider an FG calculation of nitrous oxide (N_2O) emissions, which is of interest in this study. For discussion purposes we take an estimate of the average background N_2O emission rate from soils of $1.5 \text{ kg N-N}_2\text{O ha}^{-1} \text{ y}^{-1}$ (Kim et al., 2013),² assume a friction velocity $u_* = 0.2 \text{ m s}^{-1}$, air density $\rho_a = 1.2 \text{ kg m}^{-3}$, and a dry and neutrally stratified atmosphere. For measurement heights $z_1, z_2 = (0.5, 1.5 \text{ m})$ the N_2O mole fraction difference implied by this emission rate (as per Eq. (5) given later) is 40 ppt_v: i.e., this FG measurement requires a very sensitive sensor. Even if we consider that N_2O emissions are episodic, where peak emission rates might exceed 100 times their annual average (e.g., Nyborg et al., 1997), this still requires a 1-ppb level of sensitivity. Schäfer et al. (2012) provided an example where open-path measurements were used in an FG application to measure N_2O emissions. Two ground-parallel FTIR paths were located at $z_1, z_2 = (0.5, 2.7 \text{ m})$ above a grassland surface. One of their conclusions was that the sensitivity of the FTIR limited the capability to measure N_2O fluxes.

The motivation for this work was the potential of a <1 ppb sensitive open-path FTIR (OP-FTIR) to provide N_2O and ammonia (NH_3) emission calculations from vertically separated paths. We apply the methodology described in Wilson and Flesch (2016) to cattle overwintering areas during spring snow melt (the “spring thaw”). This is a period associated with high N_2O emissions, and makes a good test of the system. It is also a logically difficult measurement environment – cattle treading on snow and ice covered ground that turns to mud – which tests the practicality of such a system. In the discussion that follows we describe the OP-FTIR system and two alternative methods to extract emissions from the measurements it provides: an FG calculation that assumes the measurements took place over a spatially infinite source, and a more rigorous inversion using a Lagrangian stochastic dispersion model (WindTrax).

2. OP-FTIR system

The University of Wollongong open path trace gas analyzer system (Bai, 2010; Laubach et al., 2013) measures the path average concentration (C_L) of several gases simultaneously by collecting and analysing the FTIR spectrum of an infra-red source that has traversed an atmospheric path. An FTIR spectrometer (Matrix-M IR cube, Bruker Optik, Ettlingen, Germany) provides modulated infrared radiation in a 25 mm diameter output beam which passes through a ZnSe beamsplitter to a beam expander constructed from a modified 12" Schmidt-Cassegrain telescope (Meade Instrument Corp., California, USA with corrector plate removed). The expanded beam follows the long open path to a 30 cm retroreflector array (PLX Industries, New York, USA) whence it returns back along the same

path to a mercury cadmium telluride detector. In this study the 1-way open path lengths ranged from 120 to 140 m. The spectrometer, beamsplitter, beam expander and detector are mounted on a 100 cm optical rail on a motorized pan-tilt tripod head (Fig. 1A) to allow the unit to be automatically aimed to different retroreflectors (Fig. 1C and D).

The spectrometer records an infrared absorption spectrum from repeated measurements over the selected averaging time (typically 2 min). Each spectrum spans a wavenumber range from 600 to 4000 cm^{-1} with a 1 cm^{-1} resolution. The spectrum is analyzed after collection using the MALT (Multiple Atmospheric Layer Transmission) software to give the line-average concentration of N_2O , NH_3 , H_2O , and other gases (Griffith, 1996; Griffith et al., 2012; Smith et al., 2011). The calculation requires atmospheric pressure and air temperature of the measurement path (see Section 2.2).

Bai (2010) reported the C_L precision (one standard deviation σ_c) of an OP-FTIR similar to ours as 0.3 and 0.4 ppb_v for N_2O and NH_3 respectively. In this study we took measurements over three days when gas concentrations were believed to be stable (pre-thaw) and calculated an average σ_c of 0.64 ppb (N_2O) and 0.41 ppb (NH_3). Given the measurements underestimate precision as they include some actual concentration variability, we interpret these as confirmation of Bai (2010) and assume a precision of 0.4 ppb (N_2O and NH_3).

2.1. Slanted paths and periscope

Emissions were calculated from the difference in C_L between two vertically offset paths (ΔC_L). Measurements were made in four configurations (2 sites \times 2 years). Three used a “slant path” configuration: the fixed OP-FTIR aimed directly at “high” and “low” reflectors that were vertically separated by about 2 m (Figs. 1C and 2) giving an average vertical path separation (Δz_{path}) of about 1 m. As a means of increasing Δz_{path} and increasing the measurement sensitivity we built a periscope to direct the lower path closer to ground (Fig. 1B). In the example cross-section of Fig. 2, the periscope increased Δz_{path} to 1.55 m (and an optimal adjustment of the periscope heights could have increased Δz_{path} to near 2 m). The periscope configuration also has the advantage of giving concentration paths nearer to parallel with ground, which simplifies an FG calculation.

The periscope was built with two 40 cm \times 60 cm flat mirrors (4–6λ first surface mirrors, Edmund Optics Inc., Barrington, NJ, USA) mounted in a frame having 3-D rotational adjustment of each mirror, adjustable separation distance between mirrors, and an adjustable height above ground. The frame was covered with corrugated plastic (Fig. 1B). The periscope was placed 4.5 m from the OP-FTIR sensor and 1.5 m off the sensor-to-reflector line. During the aiming sequence the OP-FTIR pointed directly at the high reflector to make the upper measurement, and then moved slightly in the horizontal to aim through the periscope to the lower reflector to make the lower measurement. In our emission calculations the periscope path was treated as a straight line running through the lower periscope mirror to the reflector (ignoring the geometry of the path through the periscope – although we did use the proper path length to calculate concentration).

2.2. Estimating the vertical temperature gradient

Because air temperature (T) influences the FTIR spectrum, and this is accounted for in the MALT software,³ we can improve measurement accuracy by recognizing that the measurement paths can

² Equivalent to $4.8 \text{ ng N-N}_2\text{O m}^{-2} \text{ s}^{-1}$ or $4.1 \text{ g N-N}_2\text{O ha}^{-1} \text{ d}^{-1}$.

³ Pressure also affects the FTIR spectrum, but pressure differences are very small between the path heights.



Fig. 1. Photographs of (A) the OP-FTIR unit inside a trailer (temporary box around the base insulates the aiming motor from cold); (B) the periscope; (C) the high-low reflector pair on the winter-feeding site; (D) reflectors on the winter-grazing site.

have different path-average temperatures (T_{path}) due to differences in their height. The height profile T can be calculated assuming a Monin–Obukhov (MO) similarity relationship:

$$T(z) \cong \frac{u_*^2 T_{\text{son}}}{k_v^2 g L} \left(\ln \left(\frac{z}{z_{\text{son}}} \right) - \Psi_H \left(\frac{z}{L} \right) + \Psi_H \left(\frac{z_{\text{son}}}{L} \right) \right) + T_{\text{son}}, \quad (1)$$

where u_* is the friction velocity, k_v is von Karman's constant (0.4), g is the gravitational acceleration (9.81 m s^{-2}), T_{son} is the acoustic temperature (degrees Kelvin) measured by the sonic anemometer at height z_{son} , and the stability correction is calculated as (Garratt, 1992):

$$\begin{aligned} \Psi_H \left(\frac{z}{L} \right) &= -5 \frac{z}{L} & (L > 0 : \text{ stable}) \\ &= 2 \ln \left[\left(1 + \sqrt{1 - 16z/L} \right) / 2 \right] & (L < 0 : \text{ unstable}) \end{aligned} \quad (2)$$

We calculate T_{path} by integrating Eq. (1) over the path height. This assumes equivalence between the potential temperature (described by MO relationships), acoustic temperature (measured by the sonic anemometer), and true air temperature (used in MALT). These temperatures are not the same but their height gradients are very similar (Flesch et al., 2014), and it is the temperature difference between the paths that is important in the ΔC_L calculation.

2.3. Emission calculations

We use two methods to extract N_2O and NH_3 emissions from the measured concentrations. The first is a flux-gradient (FG) method that assumes the source area extends infinitely far upwind; the second, more rigorous but (also) more cumbersome method invokes a dispersion model to compute gas trajectories from the source into the light paths, thereby taking into account the geometry of the source in relation to the detector light paths.

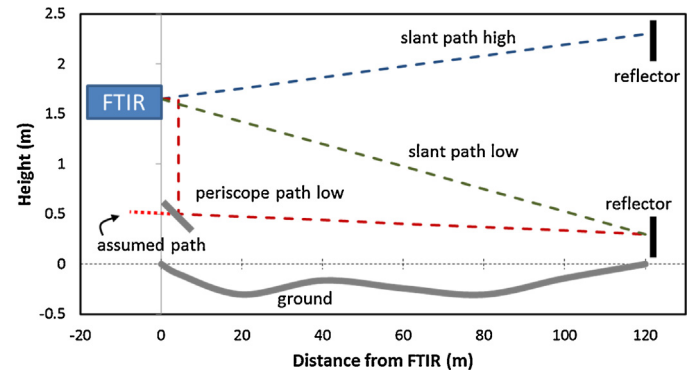


Fig. 2. Cross-section of the slant-path and periscope configurations.

2.3.1. Flux-gradient methodology

Following from Webb et al. (1980), we express the flux of gas species s in terms of the difference in mixing ratio C_s at two arbitrary heights separated by $\Delta z = z_2 - z_1$:

$$F_s = -K_s \rho_a \frac{M_s}{M_a} \frac{\Delta C_s}{\Delta z}, \quad (3)$$

where K_s is the diffusivity of gas s , ρ_a is the density of dry air, M_s and M_a are the molar masses of gas s and dry air, and ΔC_s is the difference in volumetric mixing ratio (relative to dry air) over Δz . Using this formula rather than one based on absolute concentration avoids the need for corrections for heat and water vapor fluxes (Webb et al.). We relate the gas diffusivity K_s to the eddy diffusivity for momentum (K_m) via the turbulent Schmidt number (Sc):

$$K_s = \frac{K_m}{Sc} = \frac{1}{Sc} \left(\frac{u_*^2}{\Delta U} \right) \Delta z, \quad (4)$$

where ΔU is the difference in average wind speed over Δz . There is uncertainty regarding the value of Sc . The “classic” assumption of $Sc = 1$ is commonly used (e.g., Denmead et al., 2010), however, there is evidence that $Sc < 1$ (e.g., Flesch et al., 2002; Wilson, 2013). We use $Sc = 0.64$ as indicative of studies that have deduced Sc , as well as to

be compatible with the effective Sc in the WindTrax model (Flesch et al., 2004) used later for our inverse-dispersion calculations.

Substituting Eq. (4) into Eq. (3) and expressing ΔU in terms of the stability corrected log-wind profile gives an FG formula for the surface emission rate Q_{FG} :

$$Q_{FG} = F_s = -\frac{k_v \rho_a u_* M_s}{Sc} \frac{M_a}{M_s} \left(\frac{C_s(z_2) - C_s(z_1)}{\ln\left(\frac{z_2}{z_1}\right) - \Psi_m\left(\frac{z_2}{L}\right) + \Psi_m\left(\frac{z_1}{L}\right)} \right), \quad (5)$$

where Ψ_m is a stability correction based on the Obukhov length L :

$$\begin{aligned} \Psi_m\left(\frac{z}{L}\right) &= -5 \frac{z}{L} \quad (L > 0 : \text{stable}) \\ &= 2 \ln[(1+y)/2] + \ln[(1+y^2)/2] - 2 \tan^{-1} y + \pi/2 \quad (L < 0 : \text{stable}) \end{aligned} \quad (6)$$

and $y = (1 - 16z/L)^{1/4}$.

The Q_{FG} formula in Eq. (5) applies to point measurements, whereas open-path sensors give:

$$C_L = \frac{1}{\ell_{\text{path}}} \int_{x_1}^{x_2} C_s(x, z_p) dx, \quad (7)$$

where x is the along-path horizontal coordinate (x_1 and x_2 are the horizontal positions of the sensor and the reflector), z_p is the path height above ground (allowed to be a function of x) and ℓ_{path} is the total path length. For vertically separated, but horizontally overlapping paths having the same ℓ_{path} , we integrate Eq. (5):

$$\int_{x_1}^{x_2} F_s dx = -\frac{k_v \rho_a u_* M_s}{Sc} \frac{M_a}{M_s} \int \frac{C(x, z_{p2}) - C(x, z_{p1})}{\ln\left(\frac{z_{p2}}{z_{p1}}\right) - \Psi_m\left(\frac{z_{p2}}{L}\right) + \Psi_m\left(\frac{z_{p1}}{L}\right)} dx. \quad (8)$$

With the restriction that the flux F_s is spatially uniform in the constant flux layer (i.e., the LHS of Eq. (8) is a constant) the above simplifies to our working formula for Q_{FG} :

$$\begin{aligned} Q_{FG} &= F_s \\ &= -\frac{k_v \rho_a u_* M_s}{Sc} \frac{M_a}{\ell_{\text{path}}} \frac{\Delta C_L}{\int_{x_1}^{x_2} \left[\ln\left(\frac{z_{p2}}{z_{p1}}\right) - \Psi_m\left(\frac{z_{p2}}{L}\right) + \Psi_m\left(\frac{z_{p1}}{L}\right) \right] dx}. \end{aligned} \quad (9)$$

Because the terrain at our sites was not flat we fit 2nd order polynomials to a set of path height measurements to describe $z_{p1}(x)$ and $z_{p2}(x)$. The denominator in Eq. (9) was numerically integrated for each observation period (as each period has a different L). Calculations of Q_{FG} were not made when $u_* < 0.05 \text{ m s}^{-1}$, recognizing the large uncertainty of micrometeorological inferences in very light winds.

2.3.2. Inverse dispersion methodology

Eq. (9) assumes C_L lies within the constant flux layer, which (if it is to be valid) requires an adequate upwind fetch of source. The requirement is typically expressed in terms of the ratio of the measurement height to the distance from the measurement to the upwind source boundary, and it is often taken that flux measurements require values less than 1/100. With our upper path height reaching 2.2 m, this FG fetch requirement (>220 m) is not met for some wind directions (see Fig. 4). A further requirement for an FG calculation is that the two C_L paths overlap horizontally, so that ΔC_L is not influenced by horizontal concentration gradients.

In view of the compromises (or potential sources of error) inherent in the adoption of Eq. (9), we also applied a more rigorous alternative method for calculating emissions that, in effect, best matches the concentration field provided by a suitable atmospheric

dispersion model to the observed concentrations, a so-called “inverse dispersion” method. The method is often used to calculate emissions from upwind and downwind concentrations (e.g., Harper et al., 2010). However, the approach has more generality than this. An emission rate and background concentration (C_b) can be calculated from arbitrarily located concentration pairs (where one measurement is within the emitted gas plume) – including vertically separated measurements.

For present purposes the freely available software “WindTrax” is used to make the inverse-dispersion calculations. The software takes a map of the paddock boundaries and detector paths and uses the backward Lagrangian stochastic (LS) dispersion model described by Flesch et al. (2004) to calculate the emission rate (Q_{LS}). WindTrax inputs the C_L pair and wind information (friction velocity u_* , Obukhov stability length L , the inferred surface roughness length z_0 , wind direction β , and velocity standard deviations $\sigma_{u,v,w}$) and outputs Q_{LS} and C_b . In the WindTrax calculations the height variable C_L paths are represented as best-fit linear lines with specified beginning and ending heights (only a linear height variation is allowed in the software).

Many previous inverse-dispersion studies use threshold values for u_* , L , and z_0 to remove periods where the dispersion model calculations are likely to be inaccurate. With a view to retain as many measurement periods as possible we chose to use a u_* threshold of 0.05 m s^{-1} (i.e., periods with a lower u_* are not used), which is lower than used in many previous studies. Based on the filtering study of Flesch et al. (2014) we expect this low threshold will introduce some erroneous Q_{LS} outliers but not markedly alter the accuracy of the full dataset.

There is a disadvantage to performing the inversion using the LS model. While Q_{FG} calculations take seconds, the Q_{LS} calculations can take hours. This is due to the nature of the LS model (where many thousands of trajectories are calculated for each period) and the extra calculations required to deal with height varying optical paths. If the measurement path were a constant height across the landscape, a single set of trajectories could be calculated and translated along the path to determine the required Q_{LS} – C_L relationships. But a variable path height means new trajectory sets must be calculated all along the path, reflecting the effect of varying “release” heights on trajectory properties.

3. Field measurements

The setting for our measurements is cattle overwintering areas in Alberta, Canada. Winter-feeding (WF) and winter-grazing (WG) are alternative strategies for managing cattle herds in western Canada. In WF the feed is brought to the herd (e.g., concentrated in corrals), while in WG the herd grazes a crop that has been left on the field over the winter. Winter-grazing is seen as a more economical choice as it eliminates the costs of silaging, feed hauling and storage, and equipment operation (Baron et al., 2014). It is also seen as a greenhouse gas (GHG) mitigation strategy, mainly due to the reduced fuel consumption compared with WF.

3.1. Spring thaw emissions

Over the winter cattle manure is deposited on WF and WG sites and supplies large amounts of nitrogen (N) and carbon (C) substrate to the soil. While these substrates are frozen and immobilized in the winter, in the spring they become available to a variety of chemical and biological processes that lead to emissions of nitrous oxide (N_2O) and ammonia (NH_3). In temperate agricultural soils the spring thaw is a well-known “hot-moment” of high N_2O emissions (e.g., Bremner et al., 1980; Duxbury et al., 1982; Christensen and Tiedje, 1990), where the spring emission pulse can represent the

majority of annual N_2O losses (Wagner-Riddle et al., 1997; Lemke et al., 1998; Virkajärvi et al., 2010). These pulses can be brief: on an agricultural soil in western Canada, Nyborg et al. (1997) found exceptionally large spring emissions occurred as a single event lasting about 10 days. A variety of reasons have been given for these pulses (de Bruijn et al., 2009). Two broad explanations are that: (1) during winter N_2O accumulates under the frozen soil and is released during thawing; and (2) that N_2O is newly produced (*de novo*) at a high rate in the soil surface layer as it thaws. Less is known about NH_3 emissions during thawing, as few studies have looked at this situation (Kim et al., 2012).

We expect our two sites to have different emission characteristics during thawing. In winter our WG site is generally covered by 1–3 cm of compacted ice and snow, into which is embedded fecal material, urine, and some vegetative plant residue (sources of C and N). Below this layer is a largely mineral soil having finer plant residues and some fecal matter and urine. Intermittently through the winter the compacted surface is covered with variable amounts of snow, which is tracked into (and adds to) a surface sheet of ice. As the spring thaw progresses there is sufficient water in the surface sheet to saturate the zone between the lower frozen layer and the surface, providing the conditions for denitrification and N_2O emissions. By contrast our WF surface is more variable in terms of soil moisture. Because the animals tread on an unbroken pasture and spend more time on straw bedding packs, there is less tracking and compaction, and the WF site does not develop the ice-snow surface sheet that characterizes WG fields. The firm unbroken surface at the WF site also keeps the manure from being driven into the soil by cattle treading.

One motivation for looking at open-path systems is the potential for practical measurements in difficult spring thaw conditions. The capability to remotely “look into” a snow/mud covered field can mean freedom from placing sensors in the field before winter (and the opportunity for a short campaign style visit during the thaw) or the need to fence-off cattle to keep them away from expensive sensors. And because the thawing environment is spatially inhomogeneous with patchy snow and ice cover, the large footprint of an open-path measurement can be advantageous.

3.2. Field site

Measurements took place at the Lacombe Research Centre in central Alberta (lat. 52°28'06" N, long. 113°44'13" W, elev. 870 m), an important beef production area. It has a humid continental climate with an average annual precipitation of 450 mm. Annual snowfall depth is near 1000 mm. The winters are cold and the spring thaw typically occurs in late March or early April. The study sites were on black Chernozem clay loam soil having a high organic C content of 6% (0–15 cm depth).

Emissions were measured concurrently from the WF and WG sites (Figs. 3 and 4) in 2013 and 2014. The WF site was a 2.6 ha paddock (grass surface) holding about 50 animals, with feed trucked in daily and put in feed bunks. The WG site was a 5.5 ha cropped paddock where corn (2012–2013) or triticale (2013–2014) was grown over the summer, swathed in the fall, and left to graze over the winter. Cattle were moved from summer pasture into these winter paddocks in late fall and removed in the spring (late February to April). Details are given in Table 1. The WF and WG paddocks were separated by a laneway, and the OP-FTIR was positioned between the two, with pairs of reflectors within or beside each paddock (Fig. 4). The motorized OP-FTIR was sequenced to aim at each of the four reflectors in a 10-min cycle: 4 × 2 min spectra plus 4 × 30 s aiming time. The 30-min average C_L for each path was calculated from three cycles. Gas concentrations were converted to a volumetric mixing ratio with respect to dry air using H_2O measurements from the FTIR.



Fig. 3. Winter feeding (top) and winter-grazing (bottom) sites.

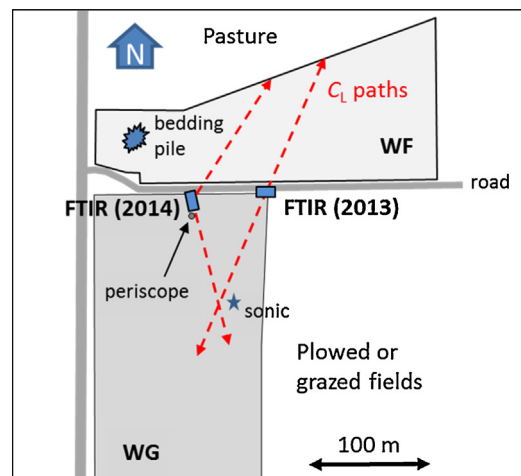


Fig. 4. Map of the study site. Measurements took place at the winter-feeding (WF) and winter-grazing (WG) sites in 2013 and 2014. The position of the OP-FTIR and concentration (C_L) measurement paths (dashed lines) was different for the two years.

A 3-D sonic anemometer (CSAT-3, Campbell Sci., Edmonton, Canada) gave the needed wind information: friction velocity u_* , Obukhov stability length L , the inferred surface roughness length z_0 , wind direction β , and velocity standard deviations ($\sigma_{u,v,w}$). The anemometer was located on the WG site at a height of either 1.97 or 1.87 m above ground. Ancillary information (soil temperatures, precipitation) was measured at a weather station approximately 1000 m from the sites.

4. Emission measurements

The OP-FTIR system was deployed over a late-March to late-April window in 2013 and 2014. There were 936 (2013) and 749 (2014) emission measurements (30-min each), representing about two-thirds and one-half of the respective deployment period. Missing measurements occurred when snow blocked the OP-FTIR paths, windstorms threatened equipment, OP-FTIR aiming misalignment,

Table 1

Details of the winter-feeding and winter-grazing sites.

	2012–2013		2013–2014	
	Winter-feeding	Winter-grazing	Winter-feeding	Winter-grazing
Area of site	2.6 ha	5.5 ha	2.6 ha	5.5 ha
Crop	–	Corn	–	Triticale
Cattle-days on site ^a	1346 ha ⁻¹	1446 ha ⁻¹	2894 ha ⁻¹	459 ha ⁻¹
Cattle feed	Barley-silage, straw	Swathed corn	Barley-silage, straw	Swathed triticale
N fertilizer rate ^b	–	55 kg N ha ⁻¹	–	92 kg N ha ⁻¹
N rate from manure	217 kg N ha ⁻¹	181 kg N ha ⁻¹	593 kg N ha ⁻¹	72 kg N ha ⁻¹
N (roots + residue)	–	82 kg N ha ⁻¹	–	172 kg N ha ⁻¹
Precipitation (September–April)	133 mm	–	173 mm	–
Soil frozen: 5 cm/20 cm	11/23 November	7/21 December	–	–
Soil thaws: 5 cm/20 cm	1/12 April	9/12 April	–	–

^a Cattle placed in paddocks in November, removed in late February–April. The low winter grazing value in 2013–2014 was due to heavy snow making it difficult for the animals to uncover the crop, and they were removed early.

^b Fertilizer applied the previous spring.

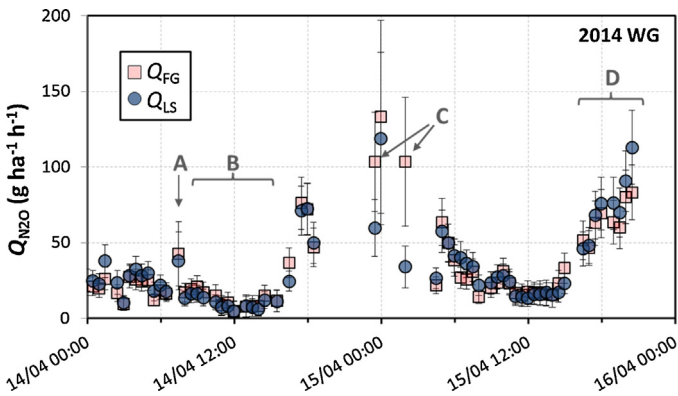


Fig. 5. Time series of N₂O emissions from the 2014 winter-grazing site. Calculations from the FG (Q_{FG}) and inverse-dispersion (Q_{LS}) techniques are shown. Error bars correspond to a $1 - \sigma$ calculation of uncertainty (see Appendix). Observations labeled A–D are discussed in the text.

etc. Of these measurement periods, roughly one-third were eliminated because $u_* < 0.05 \text{ m s}^{-1}$ or because the calculated surface roughness length z_0 exceeded the lowest reflector height.

4.1. Concentration gradients

The majority of our observations had a measurable concentration difference between the two paths (Table 2) with $|\Delta C_L|$ greater than the OP-FTIR precision estimate of 0.6 ppb (the precision of the difference ΔC_L is given by standard error propagation formula as $(2\sigma_c^2)^{1/2}$, where $\sigma_c = 0.4 \text{ ppb}$ is the precision in C_L). In most periods the sign of ΔC_L indicated gas emissions from the surface, with a small minority indicating surface deposition. The exception was NH₃ from the WG site in 2014, where deposition was indicated on about a third of the observations. It is interesting to compare ΔC_L at the WG site for the slant-path (2013) and the periscope (2014) configurations. The periscope was applied to increase ΔC_L , and this appeared to be effective, as the average $|\Delta C_L|$ doubled from 2013 to 2014 even as the emission rates were similar for the two years.

4.2. FG vs. WindTrax emission rates

Two emission calculations were made for each measurement period: a flux-gradient estimate (Q_{FG}) that neglects the impact of a finite fetch, and an inverse dispersion estimate (Q_{LS}) that does not. Fig. 5 illustrates those calculations during two days at the WG 2014 site, and identifies four periods labeled A to D for discussion. Observation “A” is judged to be an outlier for both Q_{FG} and Q_{LS} . It coincides with light winds ($u_* = 0.06 \text{ m s}^{-1}$), which leads to large uncertainty

in the effective diffusivity (see Appendix) and large uncertainty in emissions. Interval “B” shows generally good agreement between Q_{FG} and Q_{LS} , and this corresponds to southwest winds and large measurement fetches that satisfy the assumptions of FG. The interval “D” is a period of north winds with $Q_{FG} < Q_{LS}$. This difference can be explained by the short measurement fetch at the WG site during north winds, which violates the FG assumption.

There are large differences between Q_{FG} and Q_{LS} for the two nighttime observations indicated by “C” in Fig. 5. These stably stratified periods ($L \sim 5 \text{ m}$) are unusual in having relatively small vertical velocity fluctuations, with $\sigma_w/u_* = 0.57$ and 0.55 (typical values exceed 1; Kaimal and Finnigan, 1994). A low σ_w reduces the diffusivity of the atmosphere as vertical mixing is reduced relative to downwind transport. While the FG calculation (Eq. (9)) cannot accommodate this experimental information, the LS calculation does (through the input σ_w). Therefore as σ_w departs from typical values, so will Q_{FG} and Q_{LS} depart from each other. We are suspicious of both calculations under these unusual conditions, but view Q_{LS} as the better estimate: it incorporates actual turbulence information, and over our full dataset it reduces the pattern of Q_{FG} outliers during low σ_w/u_* periods.

For three of the four measurement configurations (2 sites × 2 years) the accumulated emission estimates from Q_{LS} are 10–30% higher than from Q_{FG} . The assumption that the C_L paths lie within the constant flux layer is often false at our site and this leads to Q_{FG} underestimation, i.e., $\Delta C_L/\Delta z$ is now influenced by the smaller gas flux that occurs above the constant flux layer. At the fourth position (WG 2014) the difference between Q_{FG} and Q_{LS} is less than 5%, which we attribute to the fact that for the most common wind directions (southerly) the site had large fetches more appropriate for an FG calculation.

For the reasons cited above, we view Q_{LS} as the better estimate of emissions, and focus on the Q_{LS} measurements in the following discussion.

4.3. Emission time series

Fig. 6 shows the Q_{LS} time series for N₂O (WG 2014) and NH₃ (WF 2014). Each data point in the figure is a 30-min average emission rate, and the error bars corresponding to a $1 - \sigma$ calculation of uncertainty (see the Appendix). These time series show several features common to all our measurements.

- Measurements were not continuous. Larger data gaps correspond with snow/rain/windstorms, and smaller gaps with OP-FTIR misalignment as the ground shifted during thawing.
- Emissions were generally small before the thaw. Prior to 7 April, 65% of the N₂O observations at WG 2014 are not different from

Table 2
OP-FTIR measurement details.

	2013	2014	2013	2014
	Winter-feeding	Winter-grazing	Winter-feeding	Winter-grazing
Measurement period		28 March–28 April		3 April–1 May
Emission observations	629	699	502	491
Average Δz_{path}	0.93 m	0.92 m	0.98 m	1.55 m
N₂O				
Average $ \Delta C_L $	3.6 ppb	2.9 ppb	2.0 ppb	6.9 ppb
Observations with $ \Delta C_L > 0.6 \text{ ppb}$	77%	79%	68%	78%
NH₃				
Average $ \Delta C_L $	12.5 ppb	2.1 ppb	8.1 ppb	4.2 ppb
Observations with $ \Delta C_L > 0.6 \text{ ppb}$	98%	71%	90%	88%

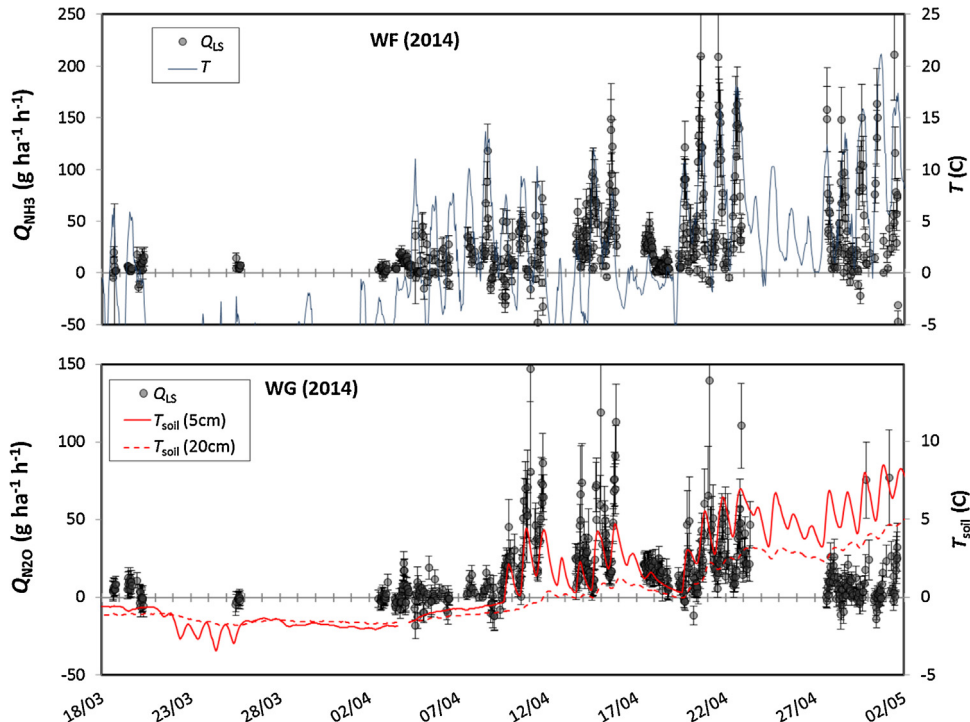


Fig. 6. Time series of emissions (Q_{LS}) of NH_3 from the winter-feeding site (top), and N_2O from the winter-grazing site (bottom) in 2014. Air (T) and soil temperatures (T_{soil}) are also shown. Error bars correspond to a $1 - \sigma$ calculation of uncertainty (see Appendix).

zero (i.e., $|Q_{\text{LS}}| - \sigma < 0$), and the average $Q_{\text{LS}} = 1.5 \text{ g N}_2\text{O ha}^{-1} \text{ h}^{-1}$. Thereafter only 18% of the observations are not different from zero, and the average $Q_{\text{LS}} = 21 \text{ g N}_2\text{O ha}^{-1} \text{ h}^{-1}$.

- Emissions were temporally variable. For example, on 10–11 April the N_2O emission rate systematically increased from 0 to 150, then fell to $16 \text{ g N}_2\text{O ha}^{-1} \text{ h}^{-1}$.
- High emission rates had large uncertainties. High N_2O emissions occurred at night when u_* was generally low, resulting in large uncertainties via an uncertain diffusivity. High NH_3 emissions tended to occur in the afternoon when higher winds reduced ΔC_L , leading to large uncertainty through an uncertain ΔC_L .

Fig. 7 focuses on N_2O emissions from the WG 2014 site as thawing begins. As emissions began a rapid rise after 9 April, the visual coherence between Q_{LS} and soil temperature at the 5 cm depth (T_{soil}) is striking. Over the initial 10 days of thawing the correlation coefficient between the two was $r = 0.79$. While this same relationship was seen at the 2013 WG site, the correlation between Q_{LS} and T_{soil} was not as strong ($r = 0.44$ over the initial 10 days of thawing) – the clearer 2014 relationship may have been

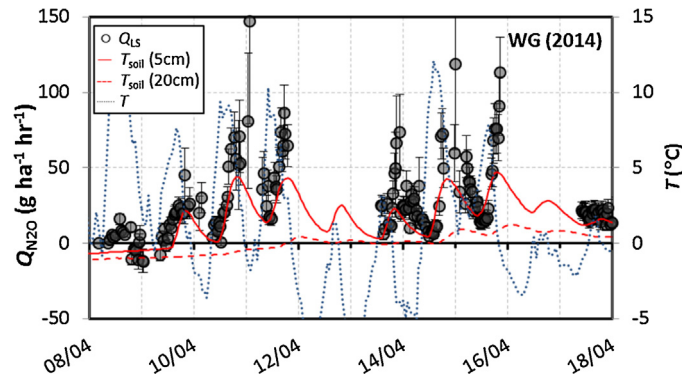


Fig. 7. Time series of N_2O emissions (Q_{LS}) from the winter-grazing site (WG) in 2014. Soil temperatures (T_{soil}) and air temperature (T) are also shown. Error bars correspond to a $1 - \sigma$ calculation of uncertainty (see Appendix).

due to use of the more sensitive periscope configuration. A strong relationship between near-surface T_{soil} and N_2O emissions over diurnal time scales has been seen by others (Williams et al., 1999; Parkin and Kaspar, 2006). Mirroring the T_{soil} cycle, maximum N_2O

emissions occurred in the evening (~20:00 LST) with minimums in the late morning (~11:00 LST). It is interesting that the emission pulse in Fig. 7 begins the day prior to T_{soil} reaching 0 °C, likely because the surface above the 5 cm depth had begun to melt. Also notice the emission pulse proceeds as the deeper soil is frozen. This has also been seen before (e.g., Flessa et al., 1995) and supports the view that de novo N_2O production in the thawed surface layer is the source of the initial pulse, and not a release of deeply trapped gas.

Emissions of NH_3 began after snow melt exposed patches of (manured) ground. Thereafter the emissions displayed a diurnal cycle positively correlated with wind speed and air temperature, resulting in sharp afternoon Q_{LS} peaks (Fig. 6). Periods of negative Q_{LS} , indicating NH_3 deposition, were mostly associated with westerly winds blowing off a pile of manure laden bedding material and into the OP-FTIR paths (Fig. 4). The pile could be a large NH_3 source that truly results in local deposition, or the effect of the pile could be misinterpreted in our methodology. A nearby NH_3 source combined with variable winds will result in large temporal variability in C_L . Because C_L from the high and low paths is measured sequentially (not concurrently), temporal variability in C_L can be falsely interpreted as vertical variability and lead to false fluxes.

5. Emission summary

Using discontinuous measurements to calculate average emissions is a challenge given the temporal variability in Q_{LS} . A gap-filling approach was used to estimate missing measurements and to provide for better time-average estimates. This was done by relying on the observed correlation between soil temperature (5 cm depth) and N_2O emissions, and between air temperature and NH_3 emissions. Missing values were calculated using a best-fit linear relationship based on Q_{LS} data within 36 h of each missing observation. This was done only for days having some Q_{LS} measurements (ignoring days without any measurements). The 30-min gap-filled record was summed to give daily emissions (Fig. 8), which were then summed to estimate the accumulated April emission losses (Table 3).

5.1. Winter-feeding site

We did not observe an N_2O emission pulse at the WF site during the thaw (unlike the WG site). Instead there was a slow rise in emissions as April progressed. Estimated April losses (Table 3) for the two years were a similar 6.9 (2013) and 6.4 (2014) kg $\text{N-N}_2\text{O ha}^{-1}$. Because of differences in manure deposition between the years, the losses are quite different when expressed as an emission factor (EF) giving the % of manure N lost as $\text{N-N}_2\text{O}$: 3.2% (2013) and 1.1% (2014). Ammonia emissions at the WF site were low until the (manured) ground was exposed by melting snow. In 2013 the rise in NH_3 emissions was rapid, quickly reaching near-maximum rates in early April, which were sustained for about 20 days before a drop-off in late April. In 2014 the emissions rose more slowly and did not peak until the later part of April, with no sign of a late-April drop-off. Total April N-NH_3 losses (Table 3) were estimated at 22.9 (2013) and 15.6 (2014) kg $\text{N-NH}_3 \text{ha}^{-1}$. When expressed as an EF for the % of manure N lost as N-NH_3 the difference between years is large: 10.6% (2013) and 2.6% (2014). The much lower 2014 EFs of both $\text{N-N}_2\text{O}$ and N-NH_3 were probably caused by the later 2014 thaw, and the yearly differences would likely have diminished if we had measured emissions into May.

5.2. Winter-grazing site

Prior to thawing the WG site was snow and ice covered, and the handful of measurements taken in March suggest emissions of N_2O and NH_3 were low prior to melting. As the soil began to thaw in

early April the N_2O emissions began. Most of the ground was snow covered when emissions began, but the surface was rapidly being exposed by melt. Commencement of the emission pulse was rapid: in 2014 the emissions rates rose from near-zero on 9 April to near-maximum on 11 April. The pulse lasted about 20 days, after which emissions rates fell to about 20% of their peak value. It seems likely that emissions continued at a lower rate after our measurements concluded. April $\text{N-N}_2\text{O}$ losses (Table 3) were 9.9 (2013) and 8.4 (2014) kg $\text{N-N}_2\text{O ha}^{-1}$. Ammonia emissions at the WG site lagged N_2O emissions by several days, beginning only after the ground was snow-free. After this the emissions continued mostly unabated until the end of the measurements. The NH_3 losses in 2013 were double those in 2014: 3.1 vs. 1.5 kg $\text{N-NH}_3 \text{ha}^{-1}$. However, when expressed as an EF giving the % of manure N lost as N-NH_3 , the two years were a similar 1.7% (2013) and 2.1% (2014).

The WF and WG sites are a contrast in terms of the form of N lost to the atmosphere. At the WF sites the N-NH_3 losses were more than twice those from $\text{N-N}_2\text{O}$, while the relationship was reversed at the WG site. This is likely due to source of available N: on the WF site manure lies on top of the grass surface, where NH_3 volatilization can rapidly proceed when warming and drying occurs; on the WG site some of the N is not available for NH_3 volatilization (from residue) and much of the manure-N that would be available has been trodden into the wet soil, which may reduce NH_3 emissions and favor N_2O production (e.g., Brink et al., 2001).

5.3. Comparison with other studies

5.3.1. N_2O emissions

Risk et al. (2013) compiled a table listing N_2O emission rates from 27 spring-thaw studies. The largest values were those measured by Nyborg et al. (1997) and Flessa et al. (1995) on cropland, with emission peaks of 137 and 42 g $\text{N}_2\text{O ha}^{-1} \text{h}^{-1}$, respectively. These can be compared with our peak rates of 134 (WF) and 195 (WG) g $\text{N}_2\text{O ha}^{-1} \text{h}^{-1}$. We thus conclude that the N_2O emission peaks we observed are among the largest spring thaw values reported. And looking at the 850+ measurements compiled in the meta-analysis of Shcherbak et al. (2014), our April N_2O loss rates are larger than 90% of the listed annual rates.

The IPCC (2006) outlines a methodology for estimating soil N_2O emissions based on the various N pools. At our sites these are the N in roots and crop residue, fertilizer, and the manure from grazing/feeding animals (Table 1). Using default emission factors (i.e., 1% for fertilizer and residue, 2% for manure) the estimated annual emissions would be 4.3 and 11.8 kg $\text{N-N}_2\text{O ha}^{-1}$ for the WF site, and 5.0 and 4.1 kg $\text{N-N}_2\text{O ha}^{-1}$ for the WG site (Table 3). In three of these four cases our April losses are larger than the IPCC annual estimates, and for the WG site the April losses are more than double the annual estimate. Do high N_2O emissions indicate problems with our measurements? There are several points to consider:

- The magnitudes of WG emissions in April are roughly similar to those measured by Nyborg et al. (1997) (e.g., 16.3 vs. 9.9 kg $\text{N-N}_2\text{O ha}^{-1}$), from a site about 100 km from ours, sharing a similar soil, climate, and N-input.
- Soil organic C was high at our WG site (6% in the 0–15 cm layer) and this has been associated with high N_2O emissions (e.g., Gagnon et al., 2011; Shcherbak et al., 2014).
- Our WG site was characterized by animals treading on tilled soil. Thomas et al. (2008) found that on wet soil (i.e., moisture levels above field capacity) this combination increased N_2O emissions by an order of magnitude over untrodden conditions.
- The daily cycle we observed in N_2O emissions (highest at 20:00, lowest at 11:00) may mean that previous thaw studies based on once-a-day chamber measurements give biased emission estimates (Williams et al., 1999). We calculate that a daily

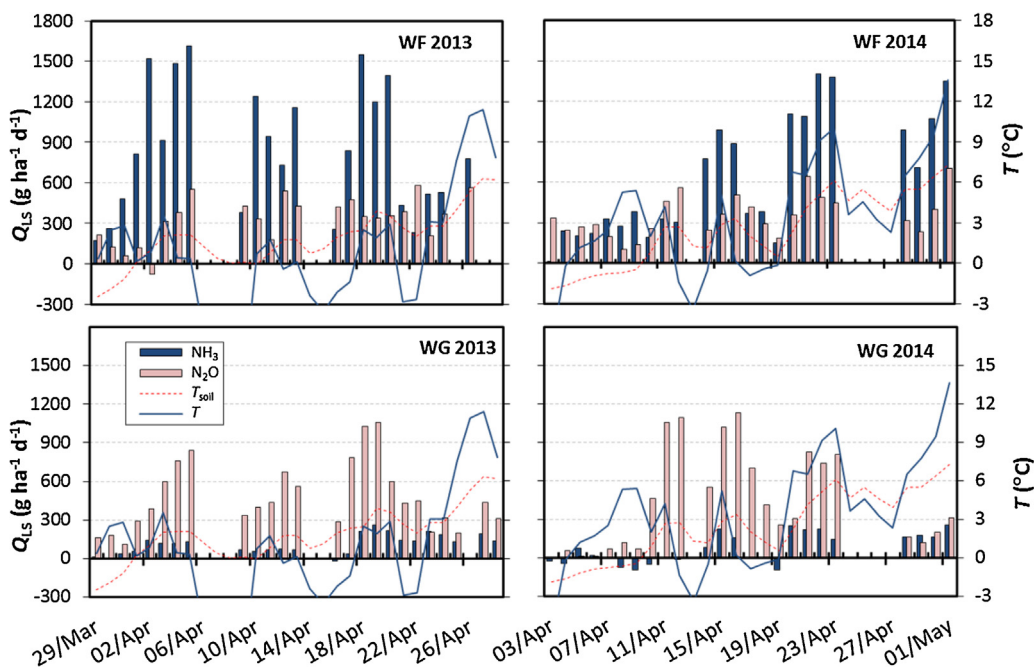


Fig. 8. Daily emission rates (Q_{ls} , in columns) of N_2O and NH_3 from the winter-grazing (WG) and winter-feeding (WF) sites in 2013 and 2014. Daily average soil temperature at 5 cm depth (T_{soil}) and air temperature (T) are given by lines. Days are 24 h periods beginning at 12:00 LST.

Table 3
Spring thaw emission losses.

	Winter-feeding		Winter-grazing	
	2013	2014	2013	2014
N_2O emissions				
April N- N_2O emission loss	6.9	6.4	9.9	8.4
$N-N_2O$ loss as % of manure N ^{a,b}	3.2%	1.1%	—	—
IPCC: annual N- N_2O emission loss ^c	4.3	11.8	5.0	4.1
NH_3 emissions				
April N- NH_3 emission loss	22.9	15.6	3.1	1.5
$N-NH_3$ loss as % of manure N ^b	10.6%	2.6%	1.7%	2.1%
April N loss ($N_2O + NH_3$)	29.8	22.0	13.0	9.9

^a Not calculated for winter grazing sites where other N pools contribute to N_2O losses (e.g., fertilizer).

^b Calculated as a % of the manure N deposited through the winter.

^c Calculation using IPCC (2006) Tier-1 methodology.

measurement taken at noon would underestimate April emissions at our WG site by about 50%.

- Our WF site has similarities to a feedlot (e.g., high animal density, high quality feed, areas of manure pack). Based on the number of cattle-days over the winter, and assuming that April emissions represent the totality of winter losses, the equivalent per-animal emission rate is 8.1 and 3.5 g N_2O animal $^{-1}$ d $^{-1}$. These are lower than the 10 and 26 g N_2O animal $^{-1}$ d $^{-1}$ found by Leytem et al. (2010) from a dairy drylot in Idaho, and Rahman et al. (2013) at a beef feedlot in North Dakota.

While our N_2O emissions were high they are not outside the bounds of what has been observed. Our WG site in particular may represent near perfect conditions for N_2O emissions during the thaw: a tilled soil with a high C content, high N input levels, and animals treading and compacting the soil surface which becomes saturated during thawing as the underlying frozen soil limits drainage.

5.3.2. NH_3 emissions

Few, if any, studies have looked at NH_3 emissions during thawing (Kim et al., 2012). Assuming winter emissions are

insignificant prior to thawing, and that manure deposited in the winter retains the potential for volatilization after thawing (Whitehead and Raistrick, 1991), we calculate a winter EF as the ratio of April N- NH_3 emissions to the manure N accumulated over the winter. At our WG site the EF is 1.7 and 2.1% (Table 3), similar to the 1.8% found by Mulvaney et al. (2008) from cattle urine in a Georgia pasture in January, but lower than the 6% and 12% found by Ball and Ryden (1984) and Sherlock and Goh (1984) from winter pastures in New Zealand. The EF was higher at our WF site, at 10.6 and 2.6% (Table 3). This was expected since the WF site has similarities to feedlots, which have much higher EFs (Koelsch and Stowell, 2005). The anomaly in our measurements is the low EF from WF 2014 (2.6%). We believe this is due to a delayed thaw in 2014 that pushed NH_3 emissions into May, after our study was finished.

6. Summary and conclusions

We judged our OP-FTIR system as capable of measuring emissions of N_2O and NH_3 from cattle overwintering areas during the spring thaw: observed emission rates were generally above the measurement threshold of the system; we saw systematic variability in emissions with environmental conditions; and the

calculated emissions were reasonably consistent with the existing scientific literature. Contributing to our success was the high level of emissions during thawing. Our system is likely to be capable of measuring high emission sites (e.g., feedlots) or high emission episodes (e.g., after fertilizer applications). However, emissions from low intensity agricultural sites or during low emitting periods of the year maybe problematic. In these cases gradient measurements based on more sensitive close-path sensors would be appropriate (e.g., Edwards et al., 2003) – with the usual close-path provisos regarding “sticky” NH₃ gas.

We also learned that N₂O emissions from our winter grazing site were large – the spring losses were among the largest that have been reported, and more than double the annual losses calculated using the IPCC (2006) methodology. We speculate this was due to the combination of high soil C levels, animal treading on tilled soil, and the addition of manure to the soil surface over the winter. While N₂O emissions were lower from the winter feeding site, they were still relatively high. The NH₃ measurements were less surprising, as the amount of manure-N being emitted as N-NH₃ was within the range seen by others.

Two methods were tested to calculate emissions from the OP-FTIR system: a flux-gradient and an inverse dispersion calculation. The inverse dispersion approach is the more flexible, as it can account for limited source fetch and arbitrary path positioning. But the computation time can be prohibitive. If measurement fetches are relatively large (e.g., the ratio of path height to upwind edge < 1/20) then the FG approach can be equally good and computationally much faster.

The OP-FTIR gradient system provides the usual advantages of micrometeorological techniques for calculating emissions. The system can (in principle) make continuous emission measurements with a footprint much larger than chamber methods, and larger than micrometeorological techniques based on point measurements – we estimate a footprint of order 10,000 m² for our study. And perhaps better than other techniques, the system can make non-interference measurements. With a footprint that extends far from the equipment, the system reduces the potential that activity around the equipment alters surface conditions in the footprint. And freed from pumps and tubing, the open-path system is particularly advantageous for a “sticky” gas like NH₃. Finally, because the open-path sensor does not need to be located within the source, it can provide a logically practical option for studying difficult environments. In our case this meant that we did not need to establish sensors in the field before winter, or to plow snow to place sensors in the field during the spring, nor did we need to fence-off cattle to keep them away from an expensive sensor.

Acknowledgements

This study would not have been possible without the assistance of Cletus Sehn, Ken Grimson, and the beef crew at the Lacombe Research Station. Special thanks to Adele Obama and Dave Young for their help in the field. Funding was provided by the Canadian Agricultural Greenhouse Gases Program (AGGP). The useful comments of anonymous reviewers were appreciated.

Appendix. Uncertainty estimates

Uncertainty in our emission calculations is estimated from a simple error propagation analysis of the FG formula (Taylor, 1982). Based on Eq. (9), the relative uncertainty in the emission measurement ($\delta Q_{FG}/Q_{FG}$) is the sum in quadrature of the relative uncertainties in Sc , ΔC_L , and the integral term in the denominator

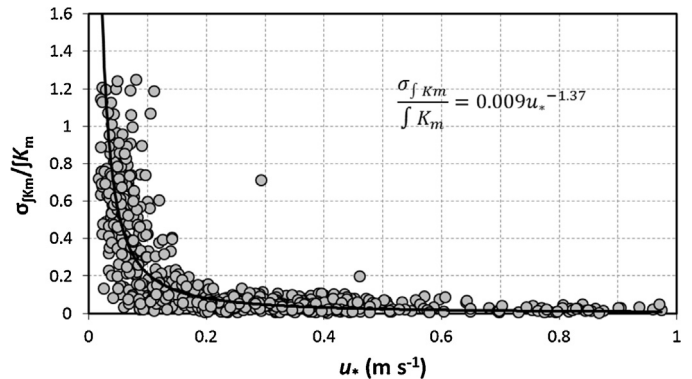


Fig. A1. Relative uncertainty in the FG diffusivity $\left(\sigma_{\int K_m} / \int K_m\right)$ plotted versus the friction velocity u_* (symbols). The given line and equation is used to describe the relationship.

(which we abbreviate $\int K_m$, as it represents uncertainty in the height integral of the diffusivity):

$$\frac{\delta Q_{FG}}{Q_{FG}} = \sqrt{\left(\frac{\delta Sc}{Sc}\right)^2 + \left(\frac{\delta(\int K_m)}{\int K_m}\right)^2 + \left(\frac{\delta(\Delta C_L)}{\Delta C_L}\right)^2}. \quad (\text{A1})$$

These uncertainties are estimated as follows:

- We use $Sc = 0.64$ and assume a relative uncertainty $\delta Sc/Sc = 0.20$. This does not represent the uncertainty in the average value of Sc (e.g., 1 or 0.64), but the period-to-period variability about the average value (e.g., due to the effects of stratification).
- The uncertainty in $\int K_m$ is estimated from a dataset described in Flesch et al. (2014). Three sonic anemometers were located at $z = 1, 2$, and 2.9 m above a homogeneous short-grass landscape. For 854 15-min observations the sonic anemometers provided three measures of (u_*, L) , which in principle should be identical given the homogeneous landscape, but which are not because of measurement errors, failure of Monin–Obukhov theory, or surface inhomogeneity. For each observation we calculate three $\int K_m$ values from the three (u_*, L) measurements as per the integral in Eq. (6), using path heights from our 2014 WG configuration. For each period the standard deviation of $\int K_m$ was calculated. Over all periods the average $\sigma_{\int K_m} / \int K_m = 0.24$. However, the uncertainty was strongly dependent on u_* (Fig. A1) and we assumed the following relationship,

$$\frac{\delta \int K_m}{\int K_m} = \frac{\sigma_{\int K_m}}{\int K_m} = 0.009(u_*)^{-1.37}. \quad (\text{A2})$$

- Uncertainty in ΔC_L is calculated as having two components, with

$$\frac{\delta(\Delta C_L)}{\Delta C_L} = \frac{\sqrt{2\sigma_C^2}}{\Delta C_L} + \frac{\frac{dC_L}{dT}\sigma_T}{\Delta C_L} \quad (\text{A3})$$

The first term (right hand side) is the uncertainty in ΔC_L due to the precision of the OP-FTIR. We use the Bai (2010) value of $\sigma_C = 0.4$ ppb for both N₂O and NH₃. The second term results from uncertainty in the path-average air temperatures (T_{path}) used in the MALT FTIR analysis software. The $T(z)$ profile is estimated from Eq. (1) and sonic anemometer measurements, but there is uncertainty in these estimates. Using the temperature profile observations from the Flesch et al. (2014) study described above, we calculated the error when a measured $T(2\text{ m})$ is used to estimate $T(1\text{ m})$, roughly paralleling the extrapolation we used to get T_{path} . The standard deviation of the T error (σ_T) was observed to be strongly dependent on u_* , varying from about 1 °C at

$u^* = 0.05 \text{ m s}^{-1}$ to $0.1 \text{ }^\circ\text{C}$ at $u^* = 0.5 \text{ m s}^{-1}$, and approximated by the best-fit relationship $\sigma_T = 0.045 u^{*-1.07}$. The resulting uncertainty in ΔC_L was estimated as the product of σ_T and the sensitivities of retrieved concentrations to temperature determined by MALT simulations: $dC_L/dT = 0.0038 \text{ (N}_2\text{O}), 0.0029 \text{ (NH}_3\text{)}$.

For surface emission sources like those in this study, there is equivalence between an LS model and an eddy-diffusivity representation of atmospheric transport. We use this equivalence to justify applying the above relative FG uncertainty calculations to the corresponding Q_{LS} inverse dispersion calculation (rather than estimating the uncertainty in the LS dispersion model calculations – a difficult task).

References

- Bai, M., (PhD thesis) 2010. *Methane emissions from livestock measured by novel spectroscopic techniques*. University of Wollongong, Australia, pp. 303.
- Ball, P.R., Ryden, J.C., 1984. Nitrogen relationships in intensively managed temperate grasslands. *Plant Soil* 76, 23–33.
- Baron, V.S., Doce, R.R., Basarab, J.A., Dick, C., 2014. Swath grazing triticale and corn compared to barley and a traditional winter feeding method in central Alberta. *Can. J. Plant Sci.* 94, 1125–1137.
- Bremner, J.M., Robbins, S.G., Blackmer, A.M., 1980. Seasonal variability in emission of nitrous oxide from soil. *Geophys. Res. Lett.* 7, 641–644.
- Brink, C., Kroeze, C., Klimont, Z., 2001. Ammonia abatement and its impact on emissions of nitrous oxide and methane in Europe – Part 1: Method. *Atmos. Environ.* 35, 6299–6312.
- Christensen, S., Tiedje, J.M., 1990. Brief and vigorous N_2O production by soil at spring thaw. *J. Soil Sci.* 41, 1–4.
- de Brujin, A.M.G., Butterbach-Bahl, K., Blagodatsky, S., Grote, R., 2009. Model evaluation of different mechanisms driving freeze-thaw N_2O emissions. *Agric. Ecosyst. Environ.* 133, 196–207.
- Denmead, O.T., Macdonald, B.C.T., Bryant, G., Naylor, T., Wilson, S., Griffith, D.W.T., Wang, W.T., Salter, B., White, I., Moody, P., 2010. Emissions of methane and nitrous oxide from Australian sugarcane soils. *Agric. Forest Meteorol.* 150, 748–756.
- Desjardins, R.L., Denmead, O.T., Harper, L., McBain, M., Masse, D., Kaharabata, S., 2004. Evaluation of a micrometeorological mass balance method employing an open-path laser for measuring methane emissions. *Atmos. Environ.* 38, 6855–6866.
- Duxbury, J.M., Bouldin, D.R., Terry, R.E., Tate III, R.L., 1982. Emissions of nitrous oxide from soils. *Nature* 298, 462–464.
- Edwards, G.C., Thurtell, G.W., Kidd, G.E., Dias, G.M., Wagner-Riddle, C., 2003. A diode laser based gas monitor suitable for measurement of trace gas exchange using micrometeorological techniques. *Agric. Forest Meteorol.* 115, 71–89.
- Flesch, T.K., McGinn, S.M., Chen, D., Wilson, J.D., Desjardins, R.L., 2014. Data filtering for inverse dispersion calculations. *Agric. Forest Meteorol.* 198–199, 1–6.
- Flesch, T.K., Prueger, J.H., Hatfield, J.L., 2002. Turbulent Schmidt number from a tracer experiment. *Agric. Forest Meteorol.* 111, 299–307.
- Flesch, T.K., Wilson, J.D., Harper, L.A., Crenna, B.P., Sharpe, R.R., 2004. Deducing ground-air emissions from observed trace gas concentrations: a field trial. *J. Appl. Meteorol.* 43, 487–502.
- Flessa, H., Dorsch, P., Beese, F., 1995. Seasonal variation of N_2O and CH_4 fluxes in differently managed arable soils in southern Germany. *J. Geophys. Res.* 100 (011), 23115–23124.
- Gagnon, B., Ziadi, N., Rochette, P., Chantigny, M.H., Angers, D.A., 2011. Fertilizer source influenced nitrous oxide emissions from a clay soil under corn. *Soil Sci. Soc. Am. J.* 75, 595–604.
- Garratt, J.R., 1992. *The Atmospheric Boundary Layer*. Cambridge University Press, New York, 316 pp.
- Griffith, D.W.T., 1996. Synthetic calibration and quantitative analysis of gas-phase FT-IR spectra. *Appl. Spectrosc.* 50, 59–70.
- Griffith, D.W.T., Deutscher, N.M., Caldow, C.G.R., Kettlewell, G., Rigganbach, M., Hammer, S., 2012. A Fourier transform infrared trace gas analyser for atmospheric applications. *Atmos. Meas. Tech.* 5, 2481–2498.
- Harper, L.A., Flesch, T.K., Wilson, J.D., 2010. Ammonia emissions from broiler production in the San Joaquin Valley. *Poultry Sci.* 89, 1802–1814.
- IPCC, 2006. In: Eggleston, H.S., Buendia, L., Miwa, K., Ngara, T., Tanabe, K. (Eds.), *IPCC Guidelines for National Greenhouse Gas Inventories*, Prepared by the National Greenhouse Gas Inventories Programme, 2006. IGES, Japan.
- Kaimal, J.C., Finnigan, J.J., 1994. *Atmospheric Boundary Layer Flows: Their Structure and Measurement*. Oxford University Press, New York, 289 pp.
- Kim, D.-G., Giltrap, D., Hernandez-Ramirez, G., 2013. Background nitrous oxide emissions in agricultural and natural lands: a meta-analysis. *Plant Soil* 373, 17–30.
- Kim, D.-G., Vargas, R., Bond-Lamberty, B., Turetsky, M.R., 2012. Effects of soil rewetting and thawing on soil gas fluxes: a review of current literature and suggestions for future research. *Biogeosciences* 9, 2459–2483.
- Koelsch, R., Stowell, R., 2005. Ammonia Emissions Estimator. University of Nebraska Extension, Lincoln, Nebraska <http://cnmp.unl.edu/AmmoniaEmissionsEstimator-21805.pdf>.
- Laubach, J., Bai, M., Pinera-Patiño, C.S., Phillips, F.A., Naylor, T.A., Molano, G., Rocha, E.A.C., Griffith, D.W.T., 2013. Testing the accuracy of micrometeorological techniques for detecting a change in methane emissions from a herd of cattle. *Agric. Forest Meteorol.* 176, 50–63.
- Lemke, R.L., Izaurralde, R.C., Nyborg, M., 1998. Seasonal distribution of nitrous oxide emissions from soil in the Parkland region. *Soil Sci. Soc. Am. J.* 62, 1320–1326.
- Leytem, A.B., Dungan, R.S., Bjorneberg, D.L., Koehn, A.C., 2010. Emissions of ammonia, methane, carbon dioxide, and nitrous oxide from dairy cattle housing and manure management systems. *J. Environ. Qual.* 40, 1383–1394.
- Mulvaney, M.J., Cummins, K.A., Wood, C.W., Wood, B.H., Tyler, P.J., 2008. Ammonia emissions from field-simulated cattle defecation and urination. *J. Environ. Qual.* 37, 2022–2027.
- Nyborg, M., Laidlaw, J.W., Solber, E.D., Malhi, S.S., 1997. Denitrification and nitrous oxide emissions from a Black Chernozemic soil during spring thaw in Alberta. *Can. J. Soil Sci.* 77, 153–160.
- Parkin, T.B., Kaspar, T.C., 2006. Nitrous oxide emissions from corn soybean systems in the midwest. *J. Environ. Qual.* 35, 1496–1506.
- Rahman, S., Borhan, M.S., Swanson, K., 2013. Greenhouse gas emissions from beef cattle pen surfaces in North Dakota. *Environ. Tech.* 34, 1239–1246.
- Risk, N., Wagner-Riddle, C., Furun, A., Warland, J., Blodau, C., 2013. Comparison of simultaneous soil profile N_2O concentration and surface N_2O flux measurements overwinter and at spring thaw in an agricultural soil. *Soil Sci. Soc. Am. J.* 78, 180–193.
- Schäfer, K., Grant, R.H., Emeis, S., Raabe, A., von der Heide, C., Schmid, H.P., 2012. Areal-averaged trace gas emission rates from long-range open-path measurements in stable boundary layer conditions. *Atmos. Meas. Tech.* 5, 1571–1583.
- Shcherbak, I., Millar, N., Robertson, G.P., 2014. Global metaanalysis of the nonlinear response of soil nitrous oxide (N_2O) emissions to fertilizer nitrogen. *Proc. Natl. Acad. Sci. U.S.A.* 111, 9199–9204.
- Sherlock, R.R., Goh, K.M., 1984. Dynamics of ammonia volatilization from simulated urine patches and aqueous urea applied to pasture. I. Field experiments. Initial emission of nitrous oxide from sheep urine applied to pasture soil. *Fertilizer Res.* 5, 181–185.
- Smith, T.E.L., Wooster, M.J., Tattaris, M., Griffith, D.W.T., 2011. Absolute accuracy evaluation and sensitivity analysis of OP-FTIR NLS retrievals of CO_2 , CH_4 and CO over concentrations ranging from those of ambient atmospheres to highly polluted plumes. *Atmos. Meas. Tech.* 4, 97–116.
- Taylor, J.R., 1982. *An Introduction to Error Analysis. The Study of Uncertainties in Physical Measurements*. University Science Books, Mill Valley, pp. 270.
- Thomas, S.M., Beare, M.H., Francis, G.S., Barlow, H.E., Hedderley, D.I., 2008. Effects of tillage, simulated cattle grazing and soil moisture on N_2O emissions from a winter forage crop. *Plant Soil* 309, 131–145.
- Virkajarvi, P., Maljanen, M., Saarijarvi, K., Haapala, J., Martikainen, P.J., 2010. N_2O emissions from boreal grass and grass-clover pasture soils. *Agric. Ecosyst. Environ.* 137, 59–67.
- Wagner-Riddle, C., Thurtell, G.W., King, K.M., Kidd, G.K., Beauchamp, E.G., 1997. Nitrous oxide and carbon dioxide fluxes from a bare soil using a micrometeorological approach. *J. Environ. Qual.* 25, 898–907.
- Webb, E.K., Pearman, G.I., Leuning, R., 1980. Correction of flux measurements for chemistry effects due to heat and water vapour transfer. *Q. J. R. Meteorol. Soc.* 106, 85–100.
- Whitehead, D.C., Raistrick, N., 1991. Effects of some environmental factors on ammonia volatilization from simulated livestock urine applied to soil. *Biol. Fertil. Soils* 11 (4), 279–284.
- Williams, D.L., Ineson, P., Coward, P.A., 1999. Temporal variation in nitrous oxide fluxes from urine-affected grassland. *Soil Biol. Biochem.* 31, 779–788.
- Wilson, J.D., 2013. Turbulent Schmidt numbers above a wheat crop. *Bound. Layer. Meteorol.* 148, 255–268.
- Wilson, J.D., Flesch, T.K., 2016. Generalized flux-gradient technique pairing line-average concentrations on vertically separated paths. *Agric. Forest Meteorol.* 220, 170–176.